Construction and Building Materials 133 (2017) 118–127

Contents lists available at ScienceDirect

Construction and Building Materials

journal homepage: www.elsevier.com/locate/conbuildmat

Numerical model on the stress field and multiple cracking behavior of Engineered Cementitious Composites (ECC)

Cong Lu [a,*], Christopher K.Y. Leung [a], Victor C. Li [b]

[a] The Hong Kong University of Science and Technology, Hong Kong
[b] University of Michigan, USA

HIGHLIGHTS

- The model numerically simulates the multiple-cracking process of ECC for the first time.
- The stress transferred to the matrix at various distances from the crack is derived.
- All key influential factors have been considered including chemical bond, slip-hardening, fiber rupture, and many others.
- Stress-strain curve of this material under tension was simulated which agrees well with experimental observations.
- This model provides insights into cause of the unsaturated-cracking phenomenon, which is most concerned for ECC application.

ARTICLE INFO

Article history:
Received 13 October 2016
Received in revised form 2 November 2016
Accepted 10 December 2016
Available online 23 December 2016

Keywords:
Simulation
Engineered Cementitious Composites (ECC)
Multiple cracking
Stress field
Ductility

ABSTRACT

Engineered cementitious composites (ECC) are materials exhibiting strain-hardening behavior with the formation of multiple cracks. The conditions for achieving multiple cracking have been investigated in the literature, but the sequential formation of cracks and the crack number/openings at a particular stress/strain level, are seldom studied. In this paper, a numerical model to simulate the overall stress-strain relation for an ECC member is developed. For a bridging fiber, the stress transferred to the matrix at various distances from the crack will be derived with consideration of chemical bond, slip hardening, fiber rupture and other factors. At any applied loading, the matrix stress field near the crack can be computed by summing up the stress transfer from all active fibers. With a new approach to describe the continuous variation of matrix strength along the member, the stress field in the matrix will be compared to the distributed matrix strength to determine the positions of new cracks. The strain at a given stress and the corresponding crack number and openings can then be obtained and the simulated stress-strain curve agrees well with experimental results. Insights from this model can facilitate the design of ECC with good mechanical performance as well as high durability.

1. Introduction

Engineered cementitious composites (ECC), also known as the bendable concrete, is a class of high performance cementitious composites characterized by high tensile ductility of several percent [1–4]. ECC exhibits strain hardening behavior accompanied by the formation of multiple fine cracks rather than a localized large crack as in normal concrete [1,3]. With the crack width in ECC materials controlled to very small values (usually below 50-60 μm) [5], improved resistance to water/chemical transport and hence better structural durability can be achieved [6–8].

In the design of ECC, physical behaviors at three different length scales need to be considered. These include the slip-displacement of a fiber due to the opening of a crack, the propagation of a matrix crack bridged by many fibers with different orientation and embedment lengths, and the behavior of a tensile member containing inherent crack-like defects [9–11]. Micromechanics theories for modeling single fiber behavior have been developed since the 1970s [12–15]. Based on the single fiber behavior, the crack bridging behavior with randomly distributed fibers can then be computed by averaging methods proposed in [4,16–19]. At the tensile component level, the conditions to achieve multiple cracks have been investigated in the literature [1,2,12,20].

Despite the increasing interest in understanding the behavior of ECC, few researchers have studied the development of multiple cracks in an ECC member, such as the number of cracks (which

* Corresponding author.
E-mail addresses: cluab@connect.ust.hk (C. Lu), ckleung@ust.hk (C.K.Y. Leung), vcli@umich.edu (V.C. Li).

http://dx.doi.org/10.1016/j.conbuildmat.2016.12.033
0950-0618/

governs composite ductility) and openings of cracks (which governs structural durability) at a particular stress level. In [21], the minimum crack spacing was derived without the consideration of strength variation along the member. As a result, the model predicts the simultaneous formation of cracks with uniform spacing, which is inconsistent with reality. In [22], a stochastic model with non-uniform matrix strength and fiber content was proposed to capture the influences of flaw-size determined matrix strength and fiber content on cracking behavior. With finite element method, another stochastic model [23] studied the influence of sample size which affects the inhomogeneity of material properties. Both models [22,23] emphasized the influence of material randomness, but the stress transfer (from fiber to matrix) in the vicinity of a crack, which physically determines the degree of multiple cracking, was overlooked. Recently in [24], an analytic model based on the stress transfer distance in matrix was developed to simulate the multiple cracking process. Besides non-uniform cracking strength, the effects of increasing crack opening and fiber rupture on the stress transfer have been taken into consideration. However, the strength variation in [24] was assumed to follow the Weibull distribution which varies randomly along the member, implying two neighboring sections can exhibit very different strength. This is inconsistent with test results showing the formation of cracks in one region followed by cracking in other regions, which can be explained by the fact that lower strength is resulted from local increase in porosity. This is often due to poorer compaction which happens not just along one section but within a certain region of the specimen. There is hence a correlation between the strength of neighboring sections that cannot be described by the Weibull distribution adopted in [24]. In addition, in the analytic model proposed in [24], the fiber/matrix interface is assumed to be governed by friction alone while various researchers [16,17,25] have reported the presence of chemical bond at the fiber/matrix interface. Also, slip hardening behavior [26] (i.e., the increasing in interfacial during fiber pull-out), which is significant for PVA-ECC materials, has been neglected. Adding the consideration of chemical bond and slip hardening to the analytic model inevitably leads to a more complex formulation which makes it impossible to obtain analytical solutions for integrals representing the average bridging stress from fibers under different situations (debonded, pull-out from one side, pull-out from both sides, rupture, etc.). In such a case, a numerical method needs to be introduced.

In this study, a new numerical model is developed to simulate the overall stress-strain relation for an ECC member. In this model, for a bridging fiber at a certain inclination angle, the fiber stress and the stress in matrix (resulted from interfacial stress transfer) will be derived as a function of the distance from the crack [16], where chemical bond, slip hardening behavior, effect of increasing crack opening and fiber rupture will all be considered. The stress field in the matrix near a crack can then be calculated by summing up the transfer from all the bridging fibers. In addition, a stochastic method that can account for the strength variation along the member, with correlation among neighboring sections, is proposed. By comparing the calculated stress field with the distributed matrix strength, the positions of new cracks are determined. At any given applied load, the number of cracks, the crack openings as well as the strain can all be obtained. The simulated stress-strain relation is then compared with experimental results and further analysis on the multiple cracking development and stress field evolution is conducted.

2. Stress field near a crack

When a crack forms in a brittle matrix composite, the stress released by the matrix is taken up by the bridging fibers. On the cracked plane, the fibers are stretched to a high strain level while the cracked matrix relaxes to zero strain. The strain difference between fibers and matrix results in interfacial shear stress through which the additional stress in fibers is transferred back to the matrix until the strain difference is eliminated. When the interfacial shear stress is high enough, debonding and sliding will occur at the interface. For a fiber perpendicular to the crack, stress transfer occurs through (1) interfacial friction along the debonded part of the fiber, and (2) a chemical bond at the end of the debonding zone. For an inclined fiber, there is an additional stress transfer due to the frictional pulley force at the exit point of the fiber [21].

In this section, the stress transfer via interface force and pulley force is studied for a single fiber first. After dividing bridging fibers into several categories under different statuses, the stress field near a crack will then be obtained by summing up the contributions from all fibers.

2.1. Stress transfer for a single fiber

2.1.1. Debonding stage

The derivation of load-displacement relation for a single embedded fiber has been described in [13,26]. Fig. 1 shows a fiber perpendicular to a crack with an embedment length of l_e and debonded over a length l_d along which fiber slippage occurs. The frictional bond strength is denoted as τ_0 and chemical bond strength as G_d. During the debonding stage (short-range relative sliding), the single fiber bridging load (P_d) is related to the fiber displacement relative to the matrix (δ) by [16]:

$$P_d = \pi\sqrt{(\tau_0\delta + G_d)E_f d_f^3(1+\eta)/2}, \quad \text{when } \delta < \delta_0 \tag{1}$$

where $\delta_0 = 2\tau_0\ l2\ e(1+\eta)/E_f\ d_f$ represents the fiber displacement when the fiber is completely debonded, and the debonding length l_d is given by [13]:

$$l_d = \frac{P_d - \sqrt{\pi^2 G_d d_f^3 E_f(1+\eta)/2}}{\pi d_f \tau_0(1+\eta)} \tag{2}$$

2.1.2. Pullout stage

After the fiber is completely debonded from the matrix (as shown in Fig. 2), the pullout stage commences. Assuming the elastic deformation of fiber to be relatively small compared to the embedded length of fiber, the fiber length remaining in the tunnel (l_p) can be expressed as [4]:

$$l_p = l_e - \delta + \delta_0 \tag{3}$$

For some types of fibers, particularly PVA fibers, slip-hardening behavior can be observed [26]. In this study, the frictional bond strength in pullout stage is assumed to vary linearly with the slip

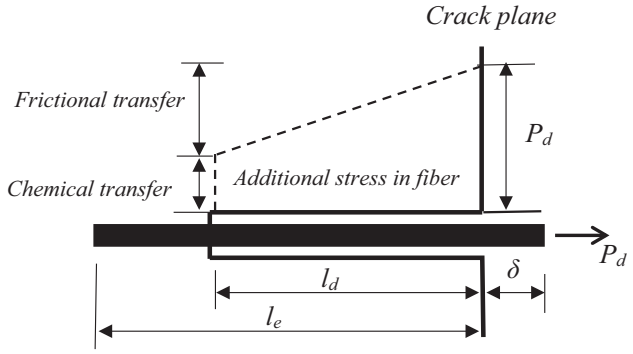

Fig. 1. Fiber in debonding stage.

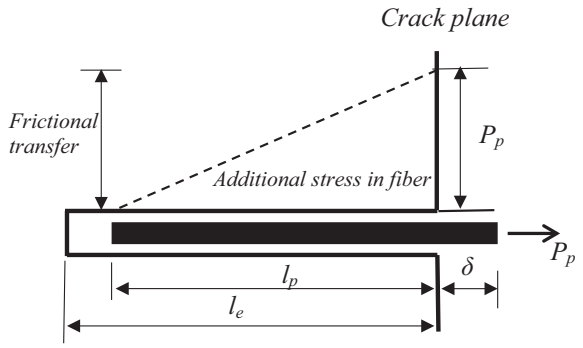

Fig. 2. Fiber in pullout stage.

distance. Taking the slip-hardening coefficient (i.e., rate of change of friction with sliding) to be β, the fiber load can then be expressed as [16]:

$$P_p = \pi\tau_0(l_e - \delta + \delta_0)(d_f + \beta(\delta - \delta_0)), \quad \text{when } \delta > \delta_0. \tag{4}$$

2.1.3. Stress transferred by pulley force

When a crack is formed and opened, a fiber at inclination angle θ will exhibit a change in angle at the exit point as shown in Fig. 3. Experimental results show an increase of crack bridging force with fiber inclination, which can be explained by the snubbing effect when the fiber (modelled as a string) is passing over a frictional pulley [27]. Assuming Coulomb friction at the pulley, it can be shown that the bridging force $P(\theta)$ for a fiber at an inclining angle θ is amplified by a factor of $e^{f\theta}$ relative to the force $P(0)$ at the other side of the fiber inside the matrix (Fig. 3). f is the snubbing coefficient to be determined experimentally. Considering force equilibrium, the force transferred to matrix along the crack opening direction by an inclined fiber at the pulley (P_{pulley}) can be derived as:

$$P_{pulley} = P(0)e^{f\theta} - P(0)\cos\theta \tag{5}$$

2.1.4. Stress transferred by interface

Away from the cracked plane, the additional stress taken by fibers will be transferred back to the surrounding matrix through the fiber/matrix interface.

For a fiber in debonding stage, the stress can be transferred by a frictional force within the debonded length l_d in Eq. (2) with a transfer rate of $\pi d_f \tau_0$, and also by the chemical bond strength G_d at the ending point of the debonding zone. Therefore, at a particular distance x from the cracked section, if x is within the debonding zone range $l_d \cos\theta$, the transfer is only via frictional force which is equal to $x\pi d_f \tau_0$. Otherwise, if x is larger than the debonding zone range $l_d \cos\theta$, the additional force $P_d \cos\theta$ in the fiber will be fully transferred back to the matrix by both frictional and chemical bond at this distance x.

For a fiber in pullout stage, the transfer occurs within the fiber length that is still in contact with the matrix, denoted as l_p in Eq. (3), with a transfer rate of $\pi(d_f + \beta(u - u_0))\tau_0$. Similarly, if x is within the reaching range of the fiber which is equal to $(l_e - u + u_0)\cos\theta$, the stress transferred by the frictional force is $x\pi(d_f + \beta(u\text{-}u_0))\tau_0$. Otherwise, the additional force $P_p \cos\theta$ will be fully transferred back to the matrix.

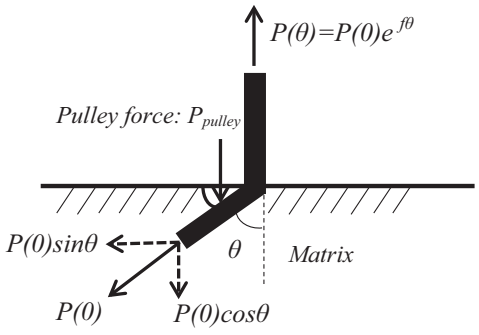

Fig. 3. Schematic diagram for snubbing effect at exit point.

2.1.5. Fiber statuses considering Two-way pullout

For fibers that do not exhibit slip hardening behavior, when the side with shorter embedded length is completely debonded, the longer embedded side remains anchored and will never enter the pullout stage as the fiber force decreases with the pullout of short side. However, for the PVA fiber, slip hardening behavior results in the possibility of two way pullout, i.e., both sides could be pulled out simultaneously if the pullout load is increased to sufficiently high values due to interfacial slip hardening on the short side [16]. In this case, the load-displacement relations for both the long and short sides of a fiber are shown in Fig. 4 and five different statuses of a fiber are defined as below to better describe the various stress transfer conditions.

(1) Two-way debonding: As shown in Fig. 4, when the stress is lower than the stress for the short side of fiber to be fully debonded, both sides are in debonding stage with equal fiber displacement relative to the matrix, meaning that the displacements on both the long and short sides are identical and equal to half the crack opening ($COD/2$).

(2) Pullout-debonding: As can also be seen in Fig. 4, when the short side of fiber is being pulled out but the stress has not exceeded the stress for the long side of fiber to be fully debonded, the long side is still in debonding stage. In this case, the fiber relative displacements on both sides (δ_S and δ_L) need to be determined separately. Numerical method is applied, where the displacement on the short side (δ_S) is taken from 0 to COD with small step size and the displacement on the long side (δ_L) is taken as COD-δ_S. The pullout force on the short side (denoted as $P_p(\delta_S, L_S)$) and debonding force on the long side (denoted as $P_d(\delta_L, L_L)$) are then computed, where L_S and L_L are the embedment length for short side and long side respectively. The computation is iterated until the difference between $P_p(\delta_S, L_S)$ and $P_d(\delta_L, L_L)$ goes below an acceptable threshold and both δ_S and δ_L can then be determined.

(3) Two-way Pullout: As mentioned before, the pullout force of the short side can become larger than the force of the long side at full debonding due to the presence of slip hardening behavior. When this happens, both sides are in pullout stage. In this case, the following equations can be set up and solved (in the same manner as described above) to determine δ_S and δ_L:

$$\begin{cases} P_p(\delta_S, L_S) = P_p(\delta_L, L_L) \\ \delta_S + \delta_L = COD \end{cases} \tag{6}$$

(4) Ruptured: when the stress exceeds the apparent strength of fiber, the fiber will undergo rupture and cannot transfer stress any more.

(5) Pulled out: when the short side of the fiber is completely pulled out from the matrix, the fiber cannot transfer stress any more.

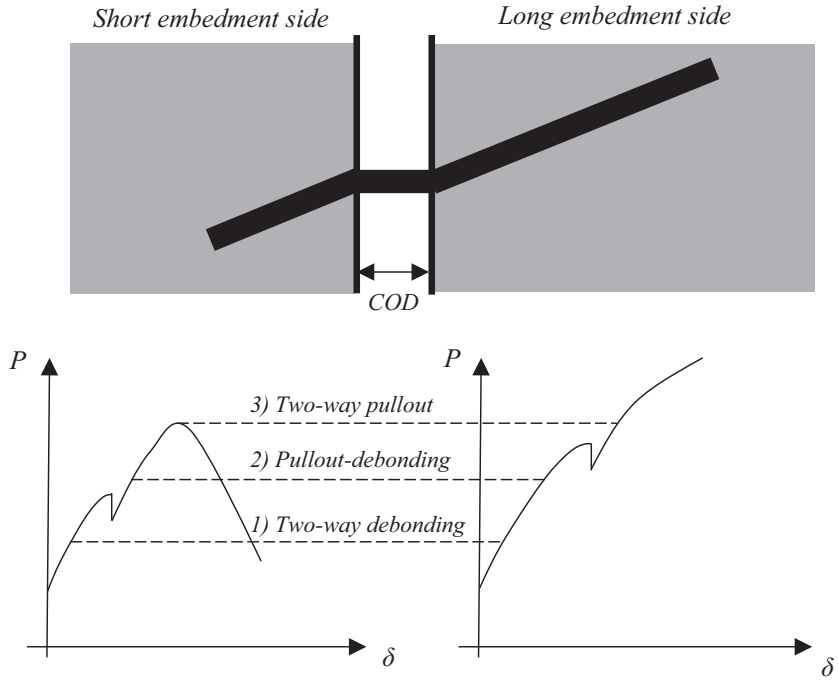

Fig. 4. Schematic diagram and load-displacement relation for both sides of a fiber.

After classifying the fibers into different statuses, the corresponding stress transfer can be calculated according to whether a particular side of the fiber is at the debonding or pullout stage. When the fiber is ruptured or completely pulled out, the fiber will be taken out from the computation.

2.2. Stress transfer for a single crack

The bridging stress and stress transfer can be calculated by summing up the contribution of all fibers. The approach adopted in [24] is to integrate analytically [24] based on the probability distributions of fiber inclination and embedment length. Adding the consideration of chemical bond and slip hardening behavior, the analytic method will give rise to tedious mathematical equations that are very difficult to integrate. A discrete method is therefore adopted in this study and the fibers are divided into groups based on the combination of their inclination angle and embedment length. The number of fibers in each group can then be calculated based on the probability distributions of inclination and embedment length. Assuming 3D randomly distribution of fibers, the embedment length on the short side can be described by a uniform distribution from 0 to $l_f/2$, while the probability density for inclination angle θ is $\sin\theta$ in the range of 0 to $\pi/2$ [15]. In reality, the distribution of fiber orientation is not truly random [28–30], in which case the experimentally determined distribution can be adopted in the model. This will be addressed in future studies.

In this study, fibers at different inclination angles are uniformly divided into 100 groups from 0 to $\pi/2$, while those with different embedment length are similarly divided into 100 groups from 0 to $l_f/2$. A total of 10,000 different groups are hence considered. The bridging stress, transferred pulley force and transferred interfacial force for each group are calculated and summed (in a weighted manner according to the probability for a fiber to be within each group) to obtain the stresses resulted from the opening of a crack, as a function of distance from the crack.

One point to be noted in the computation is that the embedment length distribution is only taken for the short embedment side from 0 to $l_f/2$, but the interfacial transfer is normally different for the long side and short side. Considering one side of a cracked plane, given the fact that fibers with long embedment length (from $l_f/2$ to l_f) shares the same distribution with the ones with short embedment length, the short side is always associated with a long side and their lengths sums up to l_f. Therefore, when calculating the frictional transfer for a certain embedment length, the frictional stress from both the long embedment side and short embedment side are calculated and averaged.

2.3. Results on stress field near a crack

To compute the stress field with the model derived above, parameters of matrix, fibers as well as the fiber/matrix interface are required. Based on the literature [16,17,26], the selected parameters for the simulation are listed in Table 1. With these parameters, the stress-crack opening relation for crack bridged by 2% fibers in volume fraction is shown in Fig. 5 and the peak strength is 5.5 MPa at about 103 μm crack opening. Based on the stress transfer analysis described above, the matrix stress field adjacent to a crack is derived and shown in Fig. 6 for various crack openings from 10 μm to 100 μm. In the figure, the stress at the crack plane represents the stress transfer due to the pulley force,

Table 1
A typical set of material parameters.

Fiber	Fiber volume fraction	2%
	Fiber length l_f (mm)	12
	Fiber diameter d_f (mm)	0.039
	Fiber elastic modulus E_f (GPa)	18
	Nominal fiber strength σ_{fu}^n (MPa)	1060
Matrix	Elastic modulus E_m (GPa)	20
	Fracture toughness K_{tip} (MPa $m^{0.5}$)	0.33
	Possoin's ratio v	0.2
Interface	Frictional bond τ_0 (MPa)	1.31
	Chemical bond strength G_d (J/m^2)	1.08
	Snubbing coefficient f	0.5
	Fiber strength reduction factor f'	0.33
	Slip Hardening Parameter β	0.58

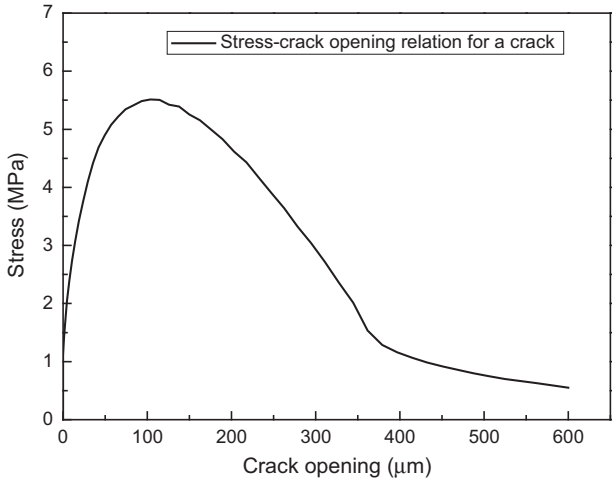

Fig. 5. Stress-cracking opening relation for a crack.

which occurs right at the crack surface. The pulley force is found to increase with increasing crack opening until the peak strength is reached. This is because the pulley stress is also increasing as the crack bridging stress is increased with crack opening.

Starting from the cracked plane, the additional stress taken by the fibers is continuously transferred back to the matrix by interfacial friction and chemical bond until the additional stress in fibers is fully transferred at a certain distance, at which the strain in both matrix and fibers becomes equal. In the case illustrated in Fig. 6, the transfer distance increases with increasing crack opening. This can be explained by the fact that larger crack opening results in higher fiber deformation and longer debonded length for fibers that have not undergone pullout. It therefore takes a longer distance for the transfer to be completed. On the other hand, with higher stress, fiber rupture and pullout are easier to occur. The transfer distance is therefore also extended by the lowered efficiency of stress transfer due to larger amount of fiber rupture and pullout as crack opening increases.

3. Modeling of non-uniform matrix strength

The classical ACK model [12] assumes uniformly distributed matrix fracture strength in the tensile member. All cracks will then form simultaneously at a uniform spacing when the matrix strength is reached. This is inconsistent with experimental observation where cracks occur sequentially and the crack spacing is random instead of being uniform. Such a physical phenomenon is caused by varying matrix strength at different sections. In [31], the non-uniform matrix strength resulted from varying flaw size was analyzed and a Weibull distribution was suggested for the matrix strength/flaw size. Such a distribution was also adopted in [24]. For the Weibull distribution, the probability for members to have a certain largest flaw/weakest section is increasing exponentially with their length, which agrees with the real situation. However, the relation of strength between adjacent sections is not considered. To illustrate this point, a Weibull distribution describing the matrix strength distribution is shown in Fig. 7. As can be seen, there is no correlation between the strength of neighboring sections so a section with very high strength can be right next to one with very low strength. However, according to experimental observation, cracking is often found to occur in a certain region of a tensile specimen first before other parts are cracked. In other words, the cracking strength is similar for neighboring sections within a weak region. This can be explained by the fact that low strength is caused by high porosity resulted from poor compaction or high local water/binder ratio, which occurs over a region of the specimen rather than at a single section. To properly describe the cracking process, a model with correlation between the strength of adjacent sections is required.

To describe this characteristic of matrix strength distribution, Kabele et al [22] suggested assuming a normal distribution for flaw size, and random locations for flaw distribution within the member. This approach is also adopted in the present study. Specifically, the member is first divided into a number of sections (In our case, the 40 mm long specimen is divided into 200 sections.). Then a number of flaws are assigned to the member and their centroid locations are taken to be randomly distributed along the length following uniform distribution. Without loss of generality, flaws are

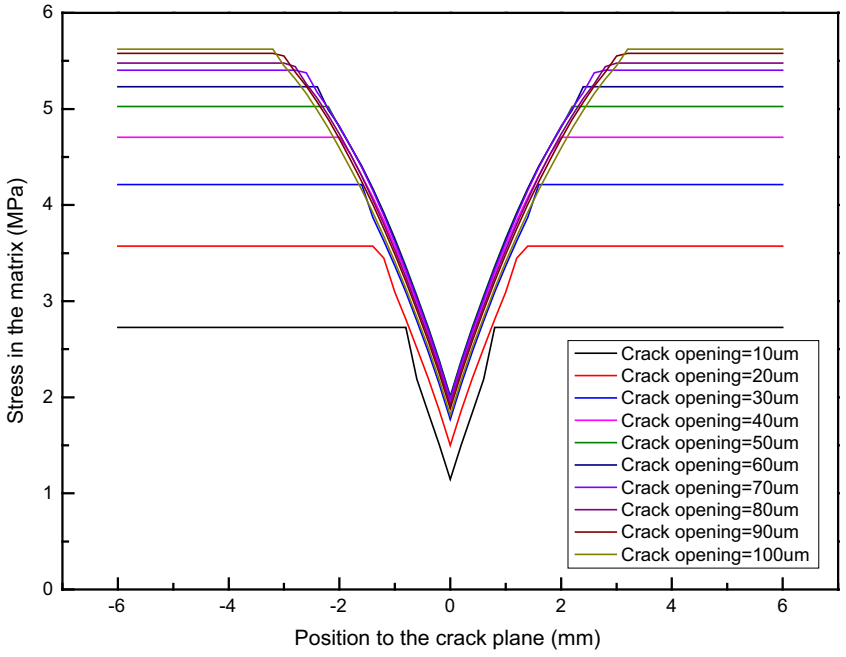

Fig. 6. Matrix stress field near a crack at various crack opening.

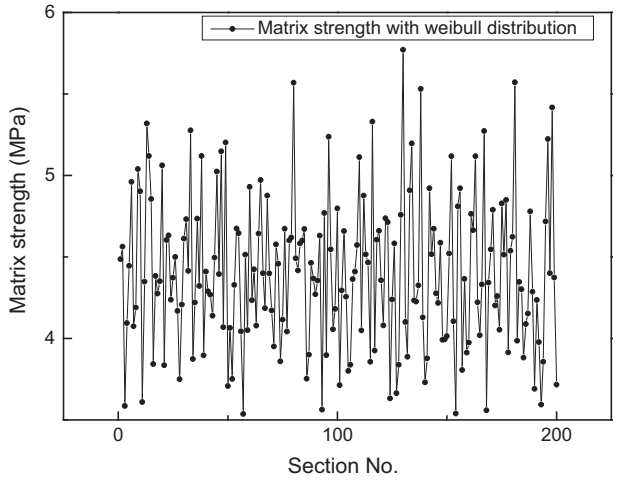

Fig. 7. Matrix strength with Weibull distribution.

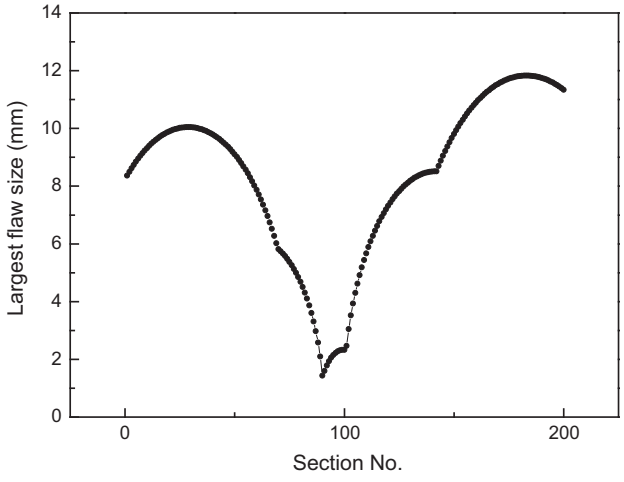

Fig. 9. Distribution of the largest flaw size along the member.

Table 2
Parameters of matrix strength distribution.

Distribution of flaw size	Mean value (mm)	4
	Standard derivation (mm)	9
Other parameters	Number of flaws	40
	Number of sections	200

assumed to be spheroidal in shape. Each flaw is then assigned a size according to normal distribution. All the assumed distribution parameters of generated flaws are listed in Table 2.

As shown in Fig. 8, several flaws with various locations and sizes are distributed in the member. Let $d_{flaw}(0)$ be the diameter of a certain flaw. For a section intersecting the flaw at a longitudinal distance of z from the middle section (see Fig. 8), the flaw diameter $d_{flaw}(z)$ can be easily calculated by:

$$d_{flaw}(z) = 2\sqrt{d_{flaw}(0)^2/4 - z^2} \tag{7}$$

Based on Eq. (7), the sizes of flaws intersected by each section can be calculated and the fracture strength is taken to be governed by the largest flaw on the section. In this manner, the dominating flaw size will vary continuously between adjacent sections as shown in Fig. 9.

Assuming the largest flaw on each section to act as a penny-shaped crack as in [4], the normalized cracking strength of the section with bridging fibers can be obtained from:

$$\tilde{\sigma}_{fc} = g\left[\frac{\sqrt{\pi}}{2}\frac{\bar{K}}{\bar{c}} + \left(\frac{4}{3}\sqrt{\bar{c}} - \frac{1}{2}\bar{c}\right)\right] \tag{8}$$

$$\text{with } g = \frac{2(1+e^{\pi f/2})}{4+f^2} \tag{9}$$

where $\tilde{\sigma}_{fc}$ stands for the first crack strength normalized by $\sigma_0 = V_f \cdot \tau_0(l_f/d_f)/2$, and V_f is the fiber volume fraction. $\bar{K}$ and $\bar{c}$ are non-dimensional quantities that indicate the normalized matrix crack tip toughness and normalized flaw size, and they are defined in [4] as:

$$\bar{K} = (K_{tip}/\sigma_0\sqrt{c_0})/(g\tilde{\delta}^*) \tag{10}$$

$$\bar{c} = \sqrt{c/c_0})/\tilde{\delta}^* \tag{11}$$

$$\text{where } c_0 = \left(\frac{l_f E_m}{2K_{tip}}\right)^2 \frac{\pi}{16(1-\nu^2)^2} \tag{12}$$

$$\text{and } \tilde{\delta}^* = \left(2\tau_0/E_f\left(1+\frac{V_f E_f}{(1-V_f)E_m}\right)\right)(L_f/d_f) \tag{13}$$

From Eqs. (8) to (13), the relation between cracking strength and flaw size can be computed. Following [4], the opening in the middle of the flaw can be related to the flaw size so the maximum bridging stress (which occurs at the middle of the flaw) for a given flaw size can be obtained. In Fig. 10, using the parameters listed in Table 1, the calculated cracking strength and maximum fiber bridging stress are plotted against the normalized flaw size $\bar{c}$. It is interesting to note that when the normalized flaw size is beyond 0.06, the cracking strength increases instead of decreasing because the second term in Eq. (8) starts to become dominant. Physically, the second term represents the bridging effect of fibers that reduces the stress intensity at the crack tip. With increasing normalized flaw size (and the corresponding crack opening), the bridging effect becomes more significant and over-compensates the increase of stress intensity due to the applied loading (which also increases with flaw size). In reality, once the maximum

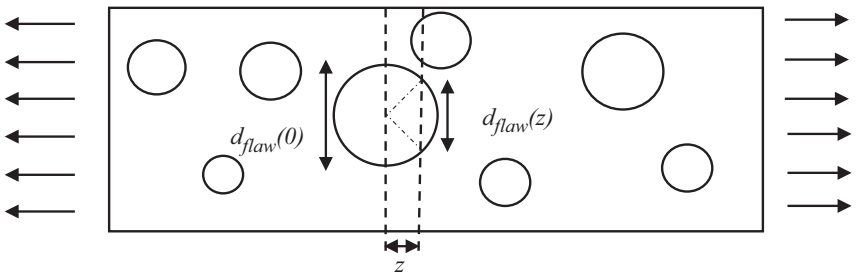

Fig. 8. Schematic diagram for calculating flaw size.

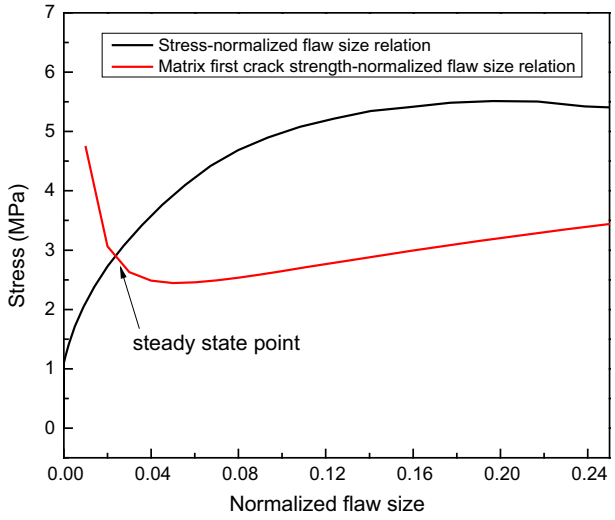

Fig. 10. First-crack strength and bridging Stress at midcrack position against normalized flaw size; intersection point indicates when the crack propagates in steady state mode.

bridging stress becomes equal to the applied stress, steady state cracking starts to occur with the maximum crack opening restricted to the value at the intersecting point and the cracking stress staying constant with further increase in flaw size. For the case illustrated in Fig. 10, the steady state cracking strength is 2.92 MPa and the corresponding normalized flaw size is 0.03.

With the parameters in Table 2, the maximum flaw size is obtained for 200 sections along the specimen as shown in Fig. 9. The cracking strength at each section is then determined from Fig. 10, with the strength becoming constant when the flaw size is larger than 49 mm (corresponding to normalized flaw size of 0.03). The variation of strength along the member is shown in Fig. 11 where the continuous variation is more representative of the real situation.

It is clear that there is some inconsistency in the above approach – spherical flaws are assumed in determining the flaw size in each section but the flaws are assumed to be penny-shaped. However, this approach can provide a better representation of real strength variation and give reasonable results for the stress vs strain curve and crack development (which will be shown in the next section). It can therefore be treated as an effective semi-empirical method to obtain a realistic strength distribution. In the above, simple assumptions have been made on the flaw shape as well as distributions of the flaw size and its centroid location. With relevant test results in the future, these aspects can be further refined to improve the model.

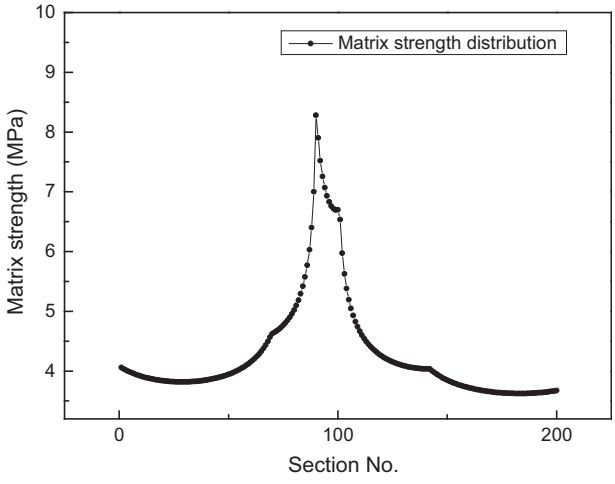

Fig. 11. Matrix strength distribution.

4. Simulation of multiple cracking process

With the distributed cracking strength and calculated stress transfer near a crack, a tensile test on ECC can be simulated. In the simulation, the stress field at each step is compared to the cracking strength distribution. If the strength is exceeded at any section, a new crack is formed. In subsequent steps, the varying matrix stress field around this new crack is recalculated from stress transfer.

As mentioned earlier, the 40 mm tensile member is divided into 200 sections (each section has a thickness of 0.2 mm). Every section is assigned a ranking number from 1 to 200, with increasing strength. Firstly, a stress equal to the strength of section 1 (weakest section) is applied. A crack opens up at section 1 and the stress field near the section is modified by stress transfer calculations.

Then, at subsequent steps, the stress is increased to the strength of the section that ranks next, until the highest strength (for section 200) is reached. When the stress is increased to the strength of a certain section (section n for instance), the new stress field at this applied stress will be recalculated. Checking for cracking will be conducted, starting from the weakest un-cracked section. If the stress field has reached its strength, a new crack will open up and the stress field should be recalculated near this section. Otherwise, this section remains un-cracked, and the section with the next lowest strength will then be checked. The flowchart for the simulation is given in Fig. 12.

If the peak bridging stress of the fiber is lower than the strength of the strongest section, the above procedure is stopped at the peak bridging stress. If the peak bridging stress turns out to be higher, the loading needs to be further increased to the failure stress (peak bridging stress). In this case, additional steps from the strength of the strongest section to the peak bridging stress will be added, and the examination procedures are similar to previous steps.

5. Results and discussion

5.1. Experimental setup

To verify the applicability of the numerical model, direct tensile tests on PVA-ECC with 2% fiber content in volume fraction was conducted on three tensile specimens. The testing set-up can be found in [32], and the part of specimen between the grips has the same length (40 mm) with the member used in the simulation. The mix proportion for the test specimens is shown in Table 3. After 28-day curing at temperature of 23 ± 2 °C, testing is performed under displacement control with the rate of 0.2 mm/min on a standard 810-Material Testing Machine. Two Linear Variable Differential Transformer (LVDT) are attached on the specimens to measure the deformation of interest zone.

5.2. Comparison between experiments and simulation

Following the simulation process, the number of cracks at each step can be obtained while the opening at each crack is directly calculated from the applied stress. The total elongation at each step due to cracking is then computed as the sum of crack opening for all the cracks (as the elastic deformation of material between the cracks is negligible compared with the crack opening). Dividing the total elongation by the specimen length, the composite strain is obtained. The simulated stress-strain curve is plotted in Fig. 13. To

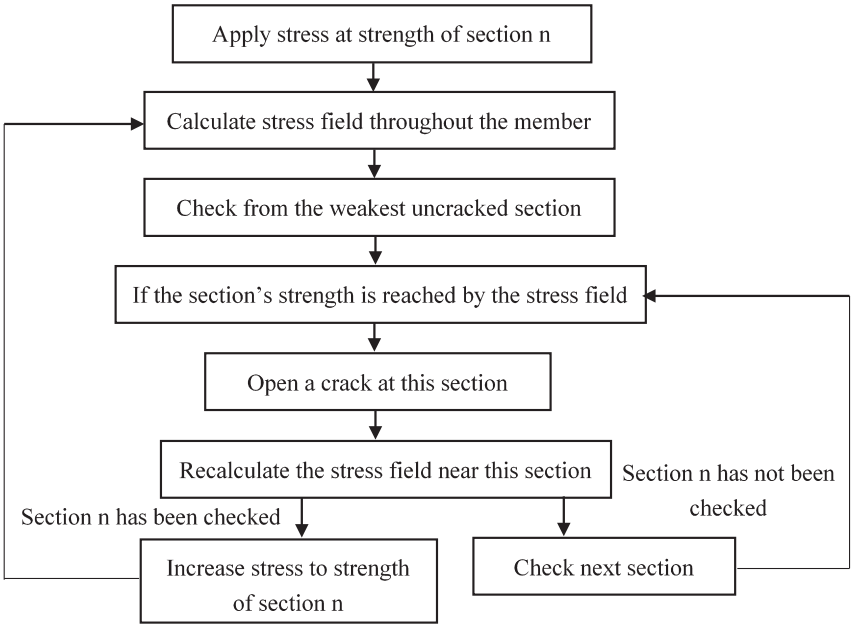

Fig. 12. Flow chart to simulate multiple cracking.

Table 3
Mix proportion for PVA-ECC.

Cement	Fly ash	Silica fume	Sand	Water	Superplasticizer	PVA fiber
0.18	0.8	0.02	0.2	0.2	0.44%	2.0%

compare, the experimental results from the three tensile specimens are also shown in Fig. 13. From the plots, the simulated strain hardening trend, first cracking strength and peak strength are very close to the test results, while the simulated ultimate strain also agree with the experiments well. As many parameters are taken from the literature and not directly measured, the purpose of the comparison is not to prove that the model can perfectly predict the tensile behavior of ECC in real situation. However, the simulation is shown to provide satisfactory prediction of the trends in real test results in many aspects.

5.3. Further discussions

The cracking sequence of multiple cracks can be obtained from the simulation results. Fig. 14 shows the cracking sequence of 22 cracks with varying section cracking strength. As can be seen, the cracking sequence does not strictly follow the ascending order of section strength. In other words, the sections with lower strength do not always crack before stronger ones. This can be explained by the stress transfer mechanism. The stress field in the member will change with the formation of cracks. For a section in the vicinity of an existing crack, while the applied stress is higher than its cracking strength, the stress transferred back to the matrix at that

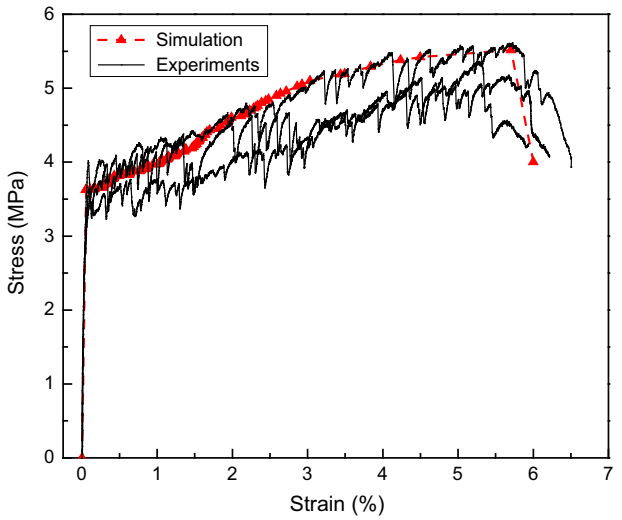

Fig. 13. Comparison of stress-strain relation from simulation and experiments.

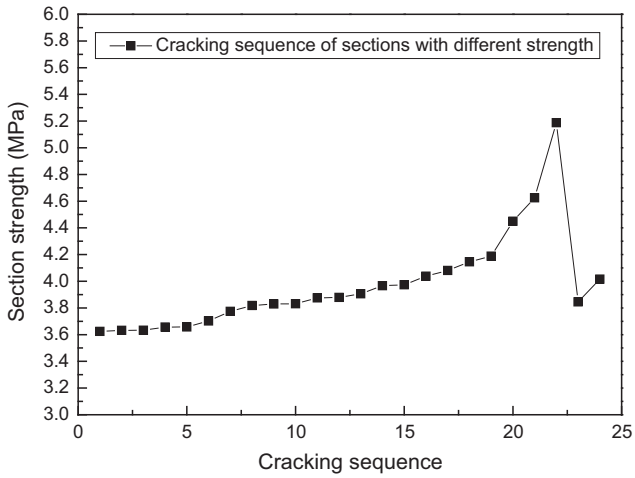

Fig. 14. Cracking sequence of 22 cracks at sections with varying strengths.

section can be lower. The section can only crack after the applied stress has further increased so the stress transfer is sufficient to induce cracking. Sections with lower strength may then crack at a later stage than stronger sections. In other words, a larger flaw shielded by the lower local stress field adjacent to a crack may be activated later in time sequence and at a lower applied load than a smaller flaw that is not shielded.

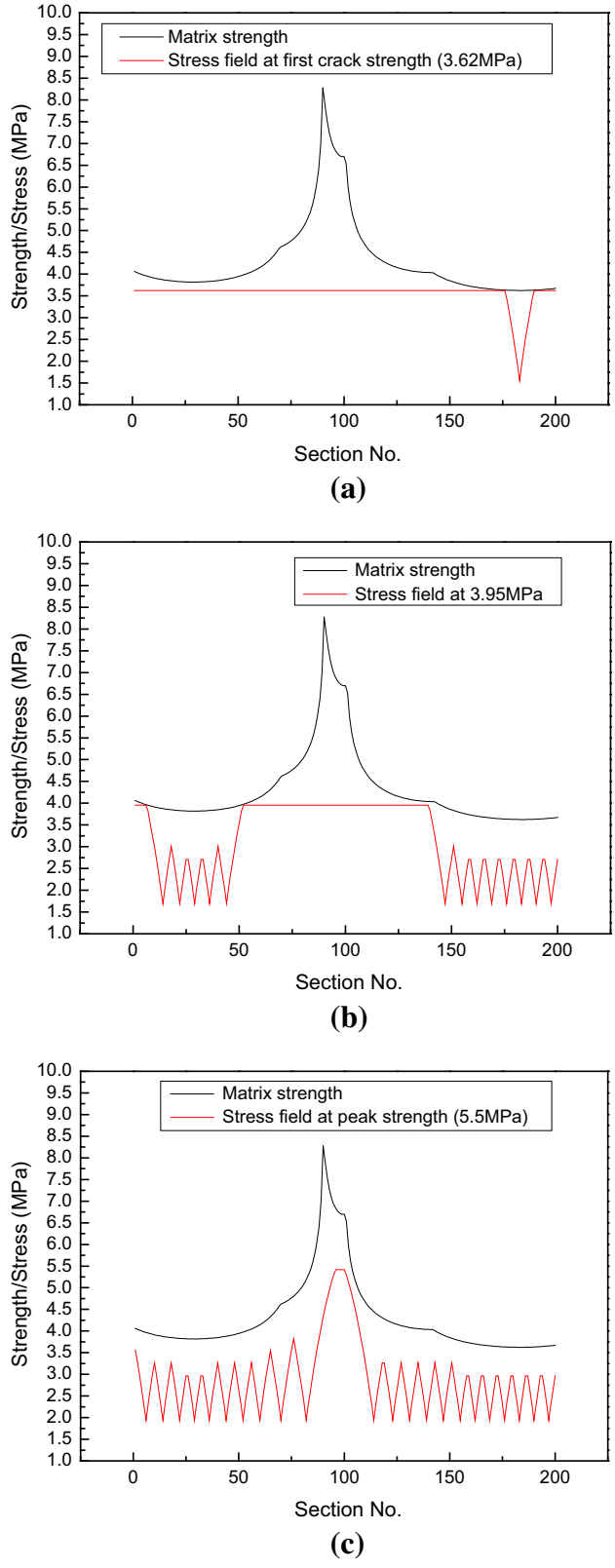

Fig. 15. Local matrix stress field and matrix strength along tensile specimen at different applied load level: (a) First crack strength; (b) 3.95 MPa; (c) Composite peak strength.

In Fig. 15, the distributed matrix strength vs stress field along the whole member is shown at three representative stages (first cracking, 3.95 MPa, and peak strength). With increasing remote stress, the cracks are getting denser and stress transfer is taking place over a larger portion of the specimen. At the latter stage, most sections of the matrix are carrying stresses transferred from the fibers and no section can truly reach the applied remote stress. This observation indicates that with more saturated multiple cracking, the fibers are more efficient in sharing the applied loading (so the matrix carries less) and this is one of the advantages of ECC members. However, as can be seen in Fig. 15b, there remains an uncracked zone in the middle portion of the specimen. This 'unsaturated cracking' becomes less significant in Fig. 15c but still exists. This is resulted from the overly high matrix cracking strength in this region as the distributed flaws in this portion are smaller than other parts. The unsaturated cracking phenomenon is often observed in ECC experiments. This model reveals the correlation between flaw distribution and regional cracking theoretically; the introduction of artificial flaws of sufficiently large size may facilitate the multiple cracking process of ECC materials as has been demonstrated in [33].

6. Conclusions

In this study, starting from the stress transfer of single fiber considering slip hardening, chemical bond, fiber rupture and other influential factors, the matrix stress field near a crack is calculated. The matrix cracking strength is distributed based on a stochastic approach that reflects the correlation of strength between neighboring sections. By comparing the local stress field with the matrix strength field at increasing remote tensile load, the formation and location of multiple cracks are determined. Stress vs strain behavior can then be derived. Simulated stress vs strain curves and crack number for a given ECC specimen was found to be in good agreement with test results.

This model provides insights into the phenomenon of unsaturated cracks where bands of microcracks are formed interspaced by bands without microcracks. This phenomenon is largely associated with segments of specimen with higher matrix strength associated with smaller flaw sizes.

Further this model reveals for the first time the conditions of microcrack forming at an applied load lower than that when the previous crack was formed. The transfer mechanism from bridging fibers into the matrix requires a distance to rebuild the matrix stress. Thus, a flaw may be shielded in this transfer zone from being one of the multiple cracks even when the remote load is high enough to cause crack initiation at this site were it not shielded.

The model developed in this work provides a framework to predict the macroscopic mechanical behavior of ECC from parameters at the microscopic level. As there are many factors that can influence the ductility and durability performance (which is dependent on crack opening and crack number) of ECC, this model can be utilized to evaluate quantitatively the effect of these factors, and hence facilitate the optimal design of ECC for various applications.

Acknowledgement

The authors would like to thank Professor Ravi Ranade at University at Buffalo for providing the program of stress-crack opening relation which this paper refers to. Also, financial support of this work by the Hong Kong Research Grant Council through GRF 615411 is gratefully acknowledged.

References

[1] V.C. Li, From Micromechanics to Structural Engineering-the Design of Cementitious Composites for Civil Engineering Applications, 1993.
[2] V.C. Li, H.-C. Wu, Conditions for pseudo strain-hardening in fiber reinforced brittle matrix composites, Appl. Mech. Rev. 45 (1992) 390–398.
[3] V.C. Li, On engineered cementitious composites (ECC), J. Adv. Concr. Technol. 1 (2003) 215–230.
[4] V.C. Li, C.K.Y. Leung, Steady-state and multiple cracking of short random fiber composites, J. Eng. Mech. 118 (1992) 2246–2264.
[5] J. Zhang, C.K. Leung, Y. Gao, Simulation of crack propagation of fiber reinforced cementitious composite under direct tension, Eng. Fract. Mech. 78 (2011) 2439–2454.
[6] M. Lepech, V.C. Li, Water permeability of cracked cementitious composites, in: Proceedings of Eleventh International Conference on Fracture, 2005, pp. 20–25.
[7] D. Hou, H. Ma, Y. Zhu, Z. Li, Calcium silicate hydrate from dry to saturated state: structure, dynamics and mechanical properties, Acta Mater. 67 (2014) 81–94.
[8] D. Hou, T. Zhao, H. Ma, Z. Li, Reactive molecular simulation on water confined in the nanopores of the calcium silicate hydrate gel: structure, reactivity, and mechanical properties, J. Phys. Chem. C 119 (2015) 1346–1358.
[9] V.C. Li, C. Wu, S. Wang, A. Ogawa, T. Saito, Interface tailoring for strain-hardening polyvinyl alcohol-engineered cementitious composite (PVA-ECC), Mater. J. 99 (2002) 463–472.
[10] V.C. Li, S. Wang, Microstructure variability and macroscopic composite properties of high performance fiber reinforced cementitious composites, Probab. Eng. Mech. 21 (2006) 201–206.
[11] C. Redon, V.C. Li, C. Wu, H. Hoshiro, T. Saito, A. Ogawa, Measuring and modifying interface properties of PVA fibers in ECC matrix, J. Mater. Civ. Eng. 13 (2001) 399–406.
[12] J. Aveston, R.A. Mercer, J.M. Sillwood, Fiber Reinforced Cements-Scientific Foundations for Specifications, Composites-Standards, Testing and Design National Physical Laboratory IPC Science and Technology Press Ltd., Guildford, Surrey, U.K., 1974, pp. 93–103.
[13] C.K. Leung, V. Li, New strength-based model for the debonding of discontinuous fibres in an elastic matrix, J. Mater. Sci. 26 (1991) 5996–6010.
[14] D. Marshall, B.N. Cox, A.G. Evans, The mechanics of matrix cracking in brittle-matrix fiber composites, Acta Metall. 33 (1985) 2013–2021.
[15] J. Aveston, A. Kelly, Theory of multiple fracture of fibrous composites, J. Mater. Sci. 8 (1973) 352–362.
[16] E.-H. Yang, S. Wang, Y. Yang, V.C. Li, Fiber-bridging constitutive law of engineered cementitious composites, J. Adv. Concr. Technol. 6 (2008) 181–193.
[17] T. Kanda, V.C. Li, Effect of fiber strength and fiber-matrix interface on crack bridging in cement composites, J. Eng. Mech. 125 (1999) 290–299.
[18] M. Maalej, V.C. Li, T. Hashida, Effect of fiber rupture on tensile properties of short fiber composites, J. Eng. Mech. 121 (1995) 903–913.
[19] V.C. Li, Postcrack scaling relations for fiber reinforced cementitious composites, J. Mater. Civ. Eng. 4 (1992) 41–57.
[20] C.K.Y. Leung, Design criteria for pseudoductile fiber-reinforced composites, J. Eng. Mech. 122 (1996) 10–18.
[21] H.C. Wu, V.C. Li, Snubbing and bundling effects on multiple crack spacing of discontinuous random fiber-reinforced brittle matrix composites, J. Am. Ceram. Soc. 75 (1992) 3487–3489.
[22] P. Kabele, M. Stemberk, Stochastic model of multiple cracking process in fiber reinforced cementitious composites, in: Proceedings of the 11th International Conference on Fracture. Turin: CCI Centro Congressi Internazionale srl, Citeseer, 2005.
[23] P. Kabele, Stochastic finite element modeling of multiple cracking in fiber reinforced cementitious composites, Fract. Damage Adv. Fibre-reinf. Cem.-based Mater. (2010) 155–163.
[24] C. Lu, C.K. Leung, A new model for the cracking process and tensile ductility of strain hardening cementitious composites (SHCC), Cem. Concr. Res. 79 (2016) 353–365.
[25] D. Hou, Y. Zhu, Y. Lu, Z. Li, Mechanical properties of calcium silicate hydrate (C–S–H) at nano-scale: a molecular dynamics study, Mater. Chem. Phys. 146 (2014) 503–511.
[26] Z. Lin, V.C. Li, Crack bridging in fiber reinforced cementitious composites with slip-hardening interfaces, J. Mech. Phys. Solids 45 (1997) 763–787.
[27] V.C. Li, Y.J. Wang, S. Backer, A micromechanical model of tension-softening and bridging toughening of short random fiber reinforced brittle matrix composites, J. Mech. Phys. Solids 39 (1991) 607–625.
[28] B.Y. Lee, J.-K. Kim, J.-S. Kim, Y.Y. Kim, Quantitative evaluation technique of Polyvinyl Alcohol (PVA) fiber dispersion in engineered cementitious composites, Cement Concr. Compos. 31 (2009) 408–417.
[29] K. Tosun-Felekoğlu, B. Felekoğlu, R. Ranade, B.Y. Lee, V.C. Li, The role of flaw size and fiber distribution on tensile ductility of PVA-ECC, Compos. B Eng. 56 (2014) 536–545.
[30] S.-I. Torigoe, T. Horikoshi, A. Ogawa, T. Saito, T. Hamada, Study on evaluation method for PVA fiber distribution in engineered cementitious composite, J. Adv. Concr. Technol. 1 (2003) 265–268.
[31] H.-C. Wu, V.C. Li, Stochastic process of multiple cracking in discontinuous random fiber reinforced brittle matrix composites, Int. J. Damage Mech. 4 (1995) 83–102.
[32] J. Yu, C.K.Y. Leung, Strength improvement of SHCC with ultra-high volumes of fly ash, in: E. Schlangen, M.G. Sierra Beltran, M. Lukovic, G. Ye (Eds.), RILEM SHCC3, RILEM S.A.R.L., Dordrecht, 2014, pp. 97–104.
[33] S. Wang, V.C. Li, Tailoring of pre-existing flaws in ECC matrix for saturated strain hardening, Proc. FRAMCOS (2004) 1005–1012.